



ORIGINAL ARTICLE

Broad spectral inhibitory effects of pale green zinc oxide nanophosphor on bacterial and fungal pathogens



H.J. Amith Yadav^a, B. Eraiah^a, H. Nagabhushana^{b,*}, B. Daruka Prasad^{c,*},
R.B. Basavaraj^b, M.K. Sateesh^{d,1}, J.P. Shabaaz Begum^d, G.P. Darshan^e,
G.R. Vijayakumar^f

^a Department of Physics, Bangalore University, Bangalore 560056, India

^b Prof. C.N.R. Rao Centre for Advanced Materials, Tumkur University, Tumkur 572103, India

^c Department of Physics, B M S Institute of Technology and Management, VTU Affiliated, Bangalore 560064, India

^d Molecular Diagnostics and Nanotechnology Laboratories, Department of Microbiology and Biotechnology, Bangalore University, Bangalore 560056, India

^e Department of Physics, Acharya Institute of Graduate Studies, Bangalore 560107, India

^f Department of Chemistry, University College of Science, Tumkur University, Tumkur 572103, India

Received 24 September 2017; accepted 13 December 2017

Available online 21 December 2017

KEYWORDS

Superstructures;
Sonochemical;
Photoluminescence;
Crop diseases;
Phytopathogens

Abstract Nd³⁺ doped zinc oxide nanophosphor were prepared by a modified sonochemical route. Adsorption of *Aloe vera* (*A.V.*) gel by the precursors made the final product with controlled morphology, that is *A.V.* gel acted as surfactant. Characterization studies confirmed the pure hexagonal phase with nanostructure, wide-bandgap was reported. Major electronic transitions in the prepared samples were due to 4f shell electrons of Nd³⁺ ions. Emission peaks attributed to ²P_{3/2} → ⁴I_{13/2}, ²P_{3/2} → ⁴I_{15/2}, ¹I₆ → ³H₄, ²P_{1/2} → ⁴I_{9/2} and ⁴G_{7/2} → ⁴I_{9/2} transitions under the excitation wavelength of 421 nm. The emitted wavelengths showed the redshift from blue to pale green region. Further, the prepared samples showed very good control over the growth of microbial pathogens such as *Staphylococcus aureus*, *Escherichia coli*, *Klebsiella pneumoniae*, *Pseudomonas aeruginosa*, *Alternaria alternata* and *Fusarium oxysporum*. The proposed mechanism is that the ZnO:Nd³⁺ interwinds the bacteria and fungal pores with a heterogeneous range of superstructures, resulting in the local perturbation at cell membrane of fungal cells. This induces to decrease the potential energy at bacterial membrane and the leakage of electrolytes of fungal spores. There is a mechanical

* Corresponding authors.

E-mail addresses: bhushanvlc@gmail.com (H. Nagabhushana), darukap@bmsit.in (B. Daruka Prasad).

¹ Deceased 10 January 2018.

Peer review under responsibility of King Saud University.



Production and hosting by Elsevier

wrapping interaction between pathogens and the nanoparticles which locally damages of the cell membrane and causes cell lysis. Biocompatible, ZnO:Nd³⁺ nanostructures possesses antibacterial activity against more multi-resistant bacterial and fungal phytopathogens. This additional information provides useful scientific information to prevent the various crop diseases.

© 2017 The Authors. Production and hosting by Elsevier B.V. on behalf of King Saud University. This is an open access article under the CC BY-NC-ND license (<http://creativecommons.org/licenses/by-nc-nd/4.0/>).

1. Introduction

In the recent years, rare-earth (RE) ions-doped semiconductors creates wide range of interest due to their unique properties and versatile applications (Ma et al., 2016; Ali et al., 2016; Guilera et al., 2016; Ramanujam and Amit, 2016; Srikesh and Samson, 2016; Sara et al., 2016; Siraj et al., 2015). Among these materials, Zinc oxide (ZnO) is used in wide range of applications viz., optical devices, piezoelectric devices, sensors, solar cells, etc., (Ghandomani et al., 2014; Mucur et al., 2015; Albiss et al., 2016; Jain et al., 2016; Bouazizi et al., 2015). Generally, crystalline shape, structure and size of ZnO nanoparticles (NPs) are greatly affected by the physic-chemical properties (Sun et al., 2016; Cheng et al., 2016). Diverse nanostructures of ZnO NPs were synthesized by various methods such as hydrothermal, solvothermal, chemical vapour deposition, ionothermal, sol-gel, direct precipitation etc., (Duo et al., 2016; Moussa et al., 2016; Sharma and Ghose, 2015; Nithya et al., 2016; Suresh et al., 2015; Chawla et al., 2012; Song et al., 2016; Wang et al., 2014). These methods demands well equipped laboratory, tedious experimental procedures and laborious experimental conditions. Hence there is a requirement of simple method of preparation with consistency in the properties of prepared products. Synthesis method which generally utilizes bio-templates permits the reaction to continue in specific conditions. Multifunctional superstructured (SS) materials can be synthesized easily because of the capability of biomolecules to form self-assembling nature with least utilization of energy. Furthermore, for the synthesis of ZnO NPs, some bio-templates have been reported as a fuel/surfactant namely extracts of fruits, leaves, barks of plants and extracts from the animals and direct use of microorganisms (Amutha et al., 2016; Ambika and Sundrarajan, 2015; Ramesh et al., 2015). In general, the bio-template may be selected for obtaining the SS and to introduce the functionality of a biological species into the inorganic materials.

Recently, an ultrasound method has been adopted to obtain micro/mesoporous materials with high-purity, size tunable, rapid reaction rate, no waste/byproduct, convenient reaction rate and the ability to get various nanostructures (NS). Extreme conditions established during ultrasonication are useful for obtaining the nano/superstructured materials. Table 1 shows the list of ZnO NS prepared by sonochemical route using different surfactants/precipitating agents. (Yu et al., 2015; Peng et al., 2015; Meshram et al., 2016; Siddiquy et al., 2012; Khataee et al., 2015a,b,c; Sharifalhoseini et al., 2015; Eskandarloo et al., 2016; Bhattacharyya and Gedanken, 2008; Khataee et al., 2016).

Aloe vera (*A. V.*) was a juicy medicinal plant, comprises of about 80 active biological and chemical constituents such as polysaccharides, enzymes, minerals, amino acids, alkaloids, flavones etc. These phytochemicals acts as bio-template and

helps in obtaining complex superstructures (SS) in the nano/micro level. Owing to these complex SS, there will be a change in the properties of the prepared compounds (Xiao and Cao, 2016).

To tune the morphology of the samples, the influential parameters such as sonication time, concentration, power and the pH of the precursor solution were optimized. Hierarchical SS were normally basic building blocks which reassemble in a well-defined manner using capping agents, surfactant molecules, bio-templates etc. (Pachauri et al., 2010) to obtain high surface to volume ratio and better properties due to charge confinement effect. Further, the photometric properties of Nd doped ZnO phosphors and their role in the inhibitory effect on the growth of pathogenic bacteria and fungi were reported.

2. Experimental

2.1. Preparation of *A.V.* gel extract

A.V. leaves were washed meticulously several times by distilled water. Inner gel of the leaves was collected carefully without contaminating. 100 ml of double distilled water was added to about 25 g of the gel and stirred well to obtain uniform homogeneous mixture. This mixture was stored in a refrigerator at 277 K for future use as a bio-template/surfactant for the preparation of ZnO.

2.2. Synthesis of ZnO: Nd³⁺ nanostructures

Pure and Nd³⁺ (0.5–9 mol %) doped ZnO SS were synthesized by using *A.V.* gel as a bio-template/surfactant via ultrasound method. Stoichiometric quantities of Neodymium (III) Nitrate {Nd(NO₃)₃} and zinc nitrate {Zn(NO₃)₂} were mixed with 50 ml of double distilled water and stirred to get a clear solution. In a separate beaker, 5 ml of *A.V.* gel extract was mixed with 100 ml double distilled water and later resultant mixture was added slowly. The resultant solution was stimulated ultrasonically for various sonication time (1–6 h). Obtained white precipitate was filtered and washed by distilled water and ethanol. Dried precipitate was used for further studies. The process of preparation was repeated for various concentrations of Nd³⁺ ions. Flowchart for the synthesis of Nd³⁺ doped ZnO SS was as shown in Fig. 1.

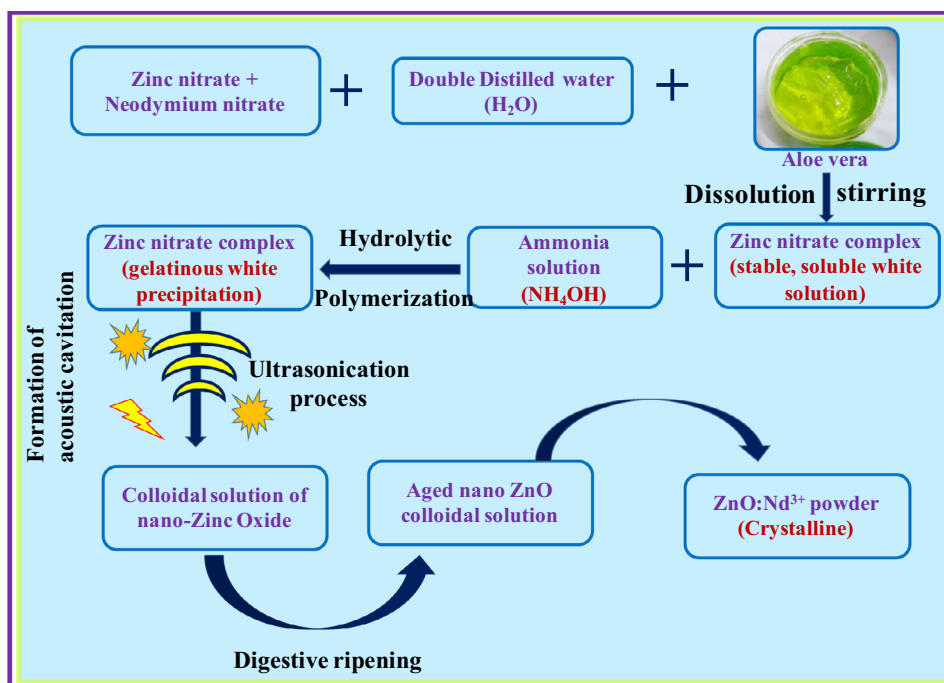
2.3. Evaluation of ZnO-Nd NPs for antibacterial activity

2.3.1. Preparation of test inoculums

The antimicrobial activity of the NPs was performed on four bacterial pathogens; one strain of gram-positive bacteria and *Staphylococcus aureus* (ATCC 6538) and three gram-negatives bacteria *Escherichia coli* (ATCC 8739), *Klebsiella*

Table 1 Pure and rare earth doped ZnO NPs prepared by sonochemical route using different precipitating agent/surfactant.

Synthesis route	Name of the precipitating/capping/surfactant agent	Name of the precursors	Crystallite size (nm)	Obtained Phases	Morphology
Sonochemical Suresh et al. (2015)	Potassium hydroxide	0.1 M Zinc chloride aqueous solution	–	Orthorhombic	Flower like
Sonochemical Chawla et al. (2012)	Diethylene glycol	Zinc acetate dihydrate	–	Hexagonal wurtzite	Randomly
Sonochemical Song et al. (2016)	KOH	Zinc acetate dehydrate, copper nitrate and sodium oxalate	231	Wurtzite	Microball
Sonochemical Wang et al. (2014)	Ethanol	Non-coated Zinc oxide	–	Zincite phase	Spherical
Sonochemical Amutha et al. (2016)	NaOH	Pr(NO ₃) ₃ ·6H ₂ O and ZnCl ₂	9	Hexagonal phase wurtzite	Spherical
Sonochemical Ambika and Sundrarajan (2015)	NaOH	Zinc acetate and Gd(NO ₃) ₃ ·6H ₂ O	–	Hexagonal phase wurtzite	Irregular shape
Sonochemical Ramesh et al. (2015)	NaOH	Zn(CH ₃ COO) ₂ ·2H ₂ O, C ₆ H ₉ EuO ₆ ·xH ₂ O and C ₂ H ₅ OH	–	Hexagonal phase wurtzite	Irregular shape
Sonochemical Yu et al. (2015)	NaOH	Er(CH ₃ COO) ₃ ·H ₂ O and ZnCl ₂	–	Hexagonal phase wurtzite	Irregular shape
Sonochemical Peng et al. (2015)	NaOH	Zinc acetate dehydrate	–	Hexagonal phase	Flower like
Sonochemical Meshram et al. (2016)	Ethanol	Zinc acetate dehydrate, samarium (1 1 1) 16 nitrate hexahydrate and oxalic dehydrate	16	Hexagonal phase Wurtzite	Spherical
Sonochemical Khataee et al. (2015)	N,N-dimethyl formamide	Zinc (II) acetate,	31	–	Micro- and Mesoporous
Sonochemical (present work)	NaOH and A.V. bio-surfactant	ZnCl ₂ and Neodymium nitrate	–	Hexagonal phase wurtzite	Irregular shape
		Zinc nitrate and Neodymium nitrate	20–40	Hexagonal phase Wurtzite	Super structures (Hexagonal, flower, pyramidal, cone etc.)

**Fig. 1** Schematic flowchart showing the synthesis of ZnO: Nd³⁺ nanostructures by ultrasonic process.

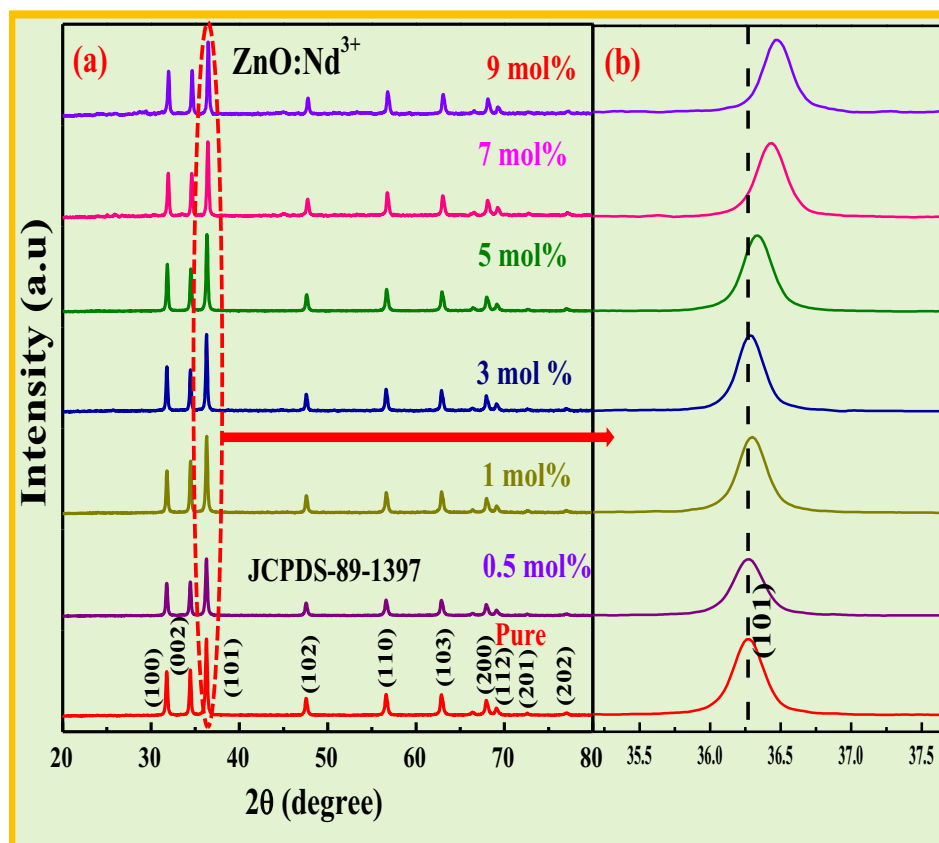


Fig. 2a PXRD profiles of pure and Nd^{3+} (0.5–9 mol %) nanostructures, (b) magnified view of peak (1 0 1) showing shift towards larger angle side.

pneumoniae (ATCC 13883) and *Pseudomonas aeruginosa* (ATCC 9027) were considered.

All the microorganisms were cultured on Mueller-Hinton (M-H) agar (Hi-Media, Mumbai, India) and incubated at 310 K for 24 h in an aerobic condition. The bacterial suspensions were prepared by selecting a single colony from the stock bacterial culture with a loop and inoculating 20 ml of sterile nutrient broth in a 100 ml of Erlenmeyer flask. The flask was then incubated in a shaking incubator at 310 K with a rotation speed of 110 rpm for 24 ± 2 h. Further, a suspension of bacterial strains with an optical density of 0.5 obtained from McFarland 1×10^8 CFU/mL was made separately in a 0.85% concentration of isotonic sodium chloride solution.

This stock solution of bacterium was diluted ten times i.e., 1×10^7 CFU/mL and used instantly for the analysis of inoculum as explained in below.

2.3.2. Measurement of the minimum inhibitory concentration (MIC) and minimum bactericidal concentration (MBC) of ZnO: Nd^{3+} NPs

Minimum inhibitory concentrations (MICs) were measured with the as gold-standard for defining the susceptibility of organisms to antimicrobial agents which was used to judge the performance of all other methods of susceptibility testing. The MIC and minimum bactericidal concentration (MBC) of the synthesized NPs under different reaction conditions were determined by broth micro-dilution method. MIC was determined according to Clinical and Laboratory Standards Institute (Ji and Zhang, 2016) with some minute modifications to use it in 96-well micro dilution plate where the bacterial strain concentration was 1×10^7 CFU/mL. A stock suspension was prepared by re-suspending the NPs in milli Q water to yield the final concentration of 100 $\mu\text{g/mL}$; the suspension is kept at 277 K. Immediately the suspension was subjected to vigorous vortex mixing, aliquots of the suspension were added into M-H medium for the further experimental procedure. To identify the potentiality of ZnO: Nd^{3+} NPs as antibacterial agent, the bacterial strains were exposed to ten-fold dilution series ranging from 25 to 2.5×10^{-5} $\mu\text{g/mL}$. The same procedure was used to determine the MIC of the positive (tetracycline), negative controls and ZnO: Nd^{3+} NPs. Tetracycline

Table 2 Estimated crystallite size, strain & energy gap values of pure & Nd^{3+} (0.5–9 mol %) doped ZnO NPs.

Nd^{3+} (mol %)	Crystallite size (nm)		Strain $\epsilon \times 10^{-3}$	Energy gap (Eg) in eV
	Scherrer's approach	W-H approach		
Pure	20	23	1.10	3.05
0.5	22	25	1.13	3.07
1	24	26	1.16	3.06
3	31	33	1.19	3.04
5	33	35	1.21	3.08
7	34	36	1.27	3.15
9	36	40	1.24	3.12

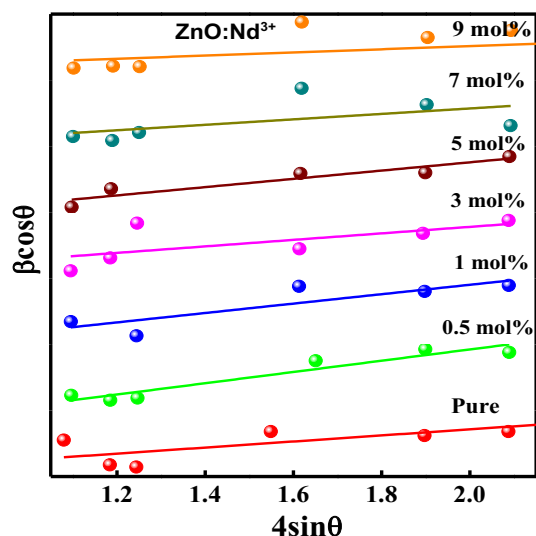


Fig. 2b Williamson–Hall plots of ZnO: Nd³⁺ (0.5–9 mol %) nanostructures.

(25 µg/mL) was considered as a standard antibiotic against the bacterial strains as a positive control. Sterile M-H broth with 0.85% of NaCl concentration was used as the negative control. MIC was defined as the lowest concentration of agent that restricted the growth to a level lower than 0.05 at 600 nm (no visible growth). The 20 µL of the bacterial suspension (10⁷ CFU/mL) was added to each well and incubated at 310 K for 24 h in a bacteriological incubator. All the tests were performed in triplicate and consequently the MIC values of the compounds were detected by the addition of 25 µL of iodinitrotetrazolium chloride (INT at 0.5 mg/mL) to each well after 24 h. The microliter plates were additionally incubated at 310 K for 60 min. MICs of each compound were determined as the lowest concentration of the NPs or drug that stopped the colour change from colorless to red. MBC determination was done by using 50 µL of cultured aliquots (without INT) was streaked onto the M-H agar in petri plates and incubated for 24 h at 310 K. The lowest concentration that indicated complete non-appearance of the bacterial growth on M-H agar surface is considered as the MBC.

Table 3 Rietveld refinement of the ZnO compound prepared with different concentration of trivalent (Nd³⁺) dopant.

	ZnO : 0.5 mol%	ZnO : 1 mol%	ZnO : 3 mol%	ZnO : 5 mol%	ZnO : 7 mol%	ZnO : 9 mol%
Crystal system	Hexagonal	Hexagonal	Hexagonal	Hexagonal	Hexagonal	Hexagonal
Space group	P 63 m c	P 63 m c	P 63 m c	P 63 m c	P 63 m c	P 63 m c
Hall Symbol	P 6c -2c	P 6c -2c	P 6c -2c	P 6c -2c	P 6c -2c	P 6c -2c
<i>Lattice parameters (Å)</i>						
a = b	3.2494	3.2482	3.2453	3.2464	3.2456	3.2506
C	5.2041	5.2027	5.1977	5.1998	5.1980	5.2042
Unit cell volume (Å ³)	47.586	47.538	47.407	47.458	47.42	46.236
<i>Atomic coordinates</i>						
<i>Zn</i>						
X	0.3333	0.3333	0.3333	0.3333	0.3333	0.3333
Y	0.6667	0.6667	0.6667	0.6667	0.6667	0.6667
Z	0.0000	0.0000	0.0000	0.0000	0.0000	0.0000
Occupancy	0.5973	0.8566	0.8571	0.8567	0.8568	0.8269
<i>Nd³⁺</i>						
X	0.3333	0.3333	0.3333	0.3333	0.3333	0.3333
Y	0.6667	0.6667	0.6667	0.6667	0.6667	0.6667
Z	0.0000	0.0000	0.0000	0.0000	0.0000	0.0000
Occupancy	0.1702	0.1693	0.0669	0.1693	0.1691	0.1691
<i>O²⁻</i>						
X	0.3333	0.3333	0.3333	0.3333	0.3333	0.3333
Y	0.6667	0.6667	0.6667	0.6667	0.6667	0.6667
Z	0.3907	0.3812	0.3729	0.3727	0.3667	0.3760
Occupancy	1.0057	1.0000	1.0011	1.0000	1.1141	1.1141
R _p	3.48	1.97	2.53	2.72	3.15	3.44
R _{WP}	5.49	2.67	4.58	4.78	5.62	5.72
R _{Exp}	3.53	3.74	2.64	4.49	4.52	4.52
χ ²	2.42	0.509	3.02	1.13	1.55	1.60
GoF	1.5	0.71	1.7	1.1	1.2	1.3
R _{Bragg}	8.37	2.98	4.21	3.29	3.93	4.77
R _F	5.66	2.45	2.47	1.90	2.30	3.61
X-ray density (g/cc ³)	5.819	5.503	5.727	5.512	5.641	5.649

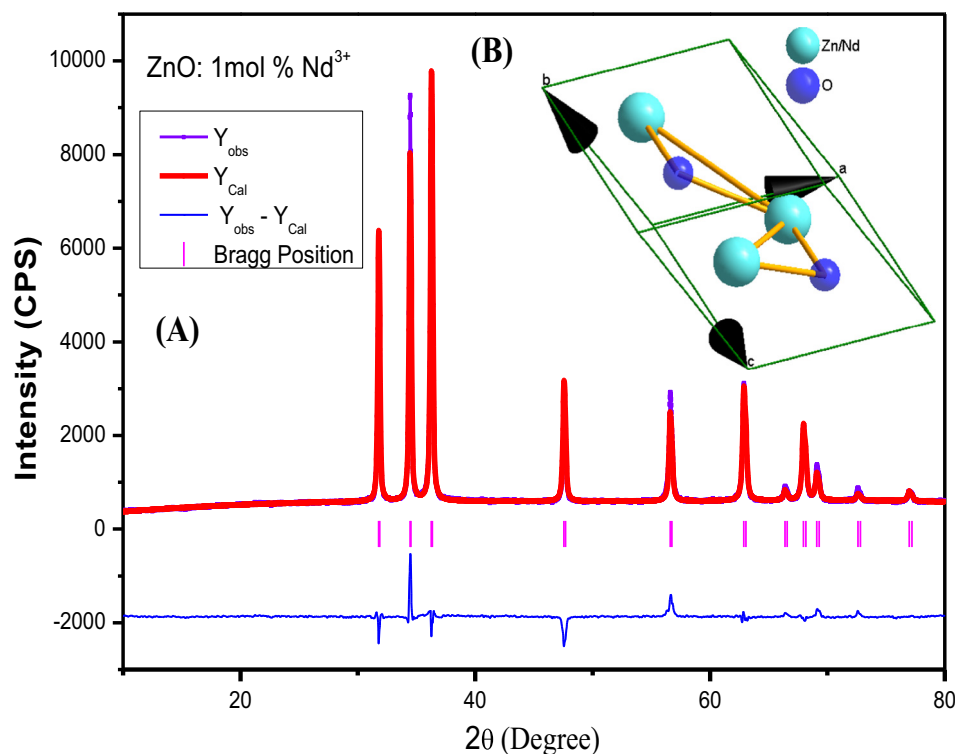


Fig. 3 (A) Rietveld refinement of 1 mol % Nd doped ZnO. (B) Inset: Packing diagram.

2.4. Antifungal activity of ZnO: Nd³⁺ NPs

The pathogenic fungi, *Alternaria alternata* (leaf spot and early blight of tomato) and *Fusarium oxysporum* (tomato blight) were procured from the culture collection centre of the Microbiology laboratory at Bangalore University, Bangalore, Karnataka, India. *Alternaria alternata* and *Fusarium oxysporum* were grown on SDA at 298 ± 10 K and incubated with alternative cycle of dark and light environment. Antifungal assay were accomplished by the agar dilution method or food poison method with slight modifications. The sterilized SDA media added with ecofriendly synthesized ZnO: Nd³⁺ NPs at 100, 200, 300, 400, 500, 600 and 700 $\mu\text{g}/\text{mL}$ concentrations and a ZnO: Nd³⁺ NPs-free media were poured into the Petri dishes (9 cm diameter). The solidified SDA media were inoculated pathogenic fungal organisms separately. The mycelial agar disc was made aseptically from the margin of 7-day-old fungal cultures with a sterile steel cork-borer (5 mm diameter). This disc was placed in the center of each Petri dish on different concentrations of ZnO: Nd³⁺ NPs and controls media. All the Petri dish with the inoculated mycelial agar disc was then incubated at 298 ± 10 K for seven days. The effectiveness of ZnO: Nd³⁺ NPs on fungal growth was assessed at the time intervals of 7 days by measuring the diameter of fungal colonies. The antifungal property of the ZnO: Nd³⁺ NPs was studied and compared with the traditional antifungal agent *nystatin*. All the experiments were done in triplicate and the values were expressed in centimeters and the antifungal index of ZnO: Nd³⁺ NPs was determined.

2.5. Statistical analysis

The antifungal experimental data was analyzed by mean \pm SE subjected to multivariate analysis. Means were separated by Duncan's multiple range tests at 0.5 significant ($P < 0.05$) using SPSS software (version 19).

2.6. Characterization

PXRD measurements were done in Shimadzu 7000 X-ray diffractometer. Hitachi – TM 3000 was used for scanning electron microscopy (SEM). Hitachi H-8100 with LaB₆ filament and Kevex sigma TM Quasar, USA were used for transmission electron microscopic (TEM) studies. The diffuse reflectance spectroscopy (DRS) of the samples was recorded on the Lambda-35 spectrometer. The spectrometer spectrum-1000 was used to perform FT-IR studies. The Jobin Yvon Spectrofluorometer Fluorolog-3 operational with 450 W Xenon lamp as an excitation source was used for photoluminescence (PL) measurement.

3. Results and discussion

3.1. PXRD analysis

PXRD patterns of the Nd³⁺ doped (0.5–9 mol %) ZnO NPs were as shown in Fig. 2a. All the profile peaks are well matched with the hexagonal phase with fine crystallinity.

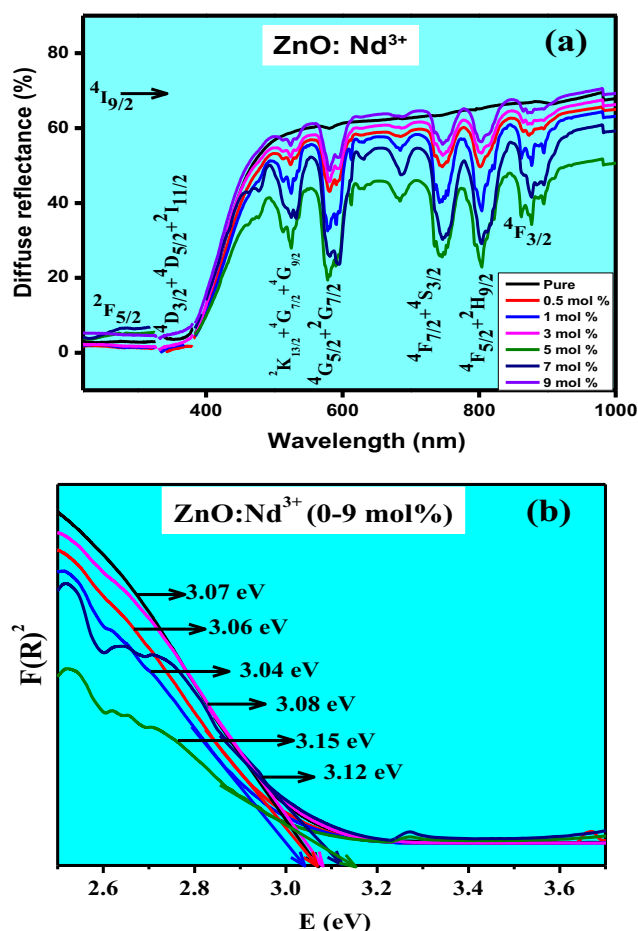


Fig. 4 (a). Diffuse reflectance spectra & (b) energy band gap plots of ZnO: Nd³⁺ (0.5–9 mol %) NPs.

Fig. 2a shows that the intensity of (0 0 1) peak is more than the intensity of (0 0 2) peak was due to the SS formation. Further, the shift in the peak position of (1 0 1) was observed with an increase in dopant concentration. All these changes were due to the stress induced by the ultrasonic waves energy moved to the crystal lattice through electron–phonon coupling (Ji and Zhang, 2016).

The acceptable percentage difference between Nd³⁺ ($R_d = 1.112 \text{ \AA}$) and Zn²⁺ ($R_s = 0.88 \text{ \AA}$) in ZnO host was and found to be 16% which is less than 30%, indicates that the dopant ions (Nd³⁺) effectively replaces Zn²⁺ ions in the ZnO host. The average crystallite size of the synthesized products was evaluated by utilizing Debye–Scherrer’s equation and was given by Basavaraj et al. (2015). The estimated values of crystallite size, strain, energy gap for the prepared samples were summarized in Table 2.

Williamson–hall (W-H) approach was used to estimate crystallite size and strain present within the prepared samples and tabulated in Table 2 (Nagabhushana et al., 2016). A straight line between $4 \sin \theta$ versus $\beta \cos \theta$ for ZnO: Nd³⁺ (0.5–9 mol %) nanophosphors (NPs) was as showed in Fig. 2b. Rietveld refinement method was quite useful to calculate the accurate structural and unit cell parameters of the compound. For this, PXRD raw data was used as input data to *FullProf* software. The refined parameters such as occupancy, atomic functional positions for ZnO: Nd³⁺ (0.5–9 mol %) were summarized

Table 3. It was observed that ZnO shows hexagonal crystal structure with lattice parameter $a = b = 3.2463 \text{ \AA}$, $c = 5.1860 \text{ \AA}$, $V = 47.43 \text{ \AA}^3$ and space group = $P63mc$. The goodness of fit defined by $\chi^2 = (R_p/R_{wp})^2$ was found to be in the range of 1.1 which confirms the good fitting (Fig. 3). Diamond software (Morozov et al., 2015; Madan et al., 2016) was utilized for showing the possible packing diagram as in inset of Fig. 3.

Fig. 4(a) depicts the DRS of pure and Nd³⁺ doped ZnO NPs at room temperature (RT). A sharp peak at $\sim 385 \text{ nm}$, attributed to the intrinsic band-gap absorption of ZnO due to the electron transitions from the valence band to the conduction band ($O_{2p} \rightarrow Zn_{3d}$). The spectra exhibited major peaks at 275, 360, 529, 586, 680, 742 and 806 nm were due to the transitions of the 4f electrons of Nd³⁺ ions from the ground-state to $4I_{9/2} \rightarrow 2F_{5/2}$, $4D_{3/2} + 4D_{5/2} + 2I_{11/2}$, $2K_{13/2} + 4G_{7/2} + 4G_{9/2}$, $4G_{5/2} + 2G_{7/2}$, $4F_{7/2} + 4S_{3/2}$, $4F_{5/2} + 2H_{9/2}$ and $4F_{3/2}$ respectively (Peng et al., 2014).

Kubelka–Munk function was utilized to determine the energy band gap (E_g) of ZnO: Nd³⁺ NPs (Zhang et al., 2012; Wan et al., 2007). The intercepts of the tangents drawn to the plots of $[F(R_\infty) hv]^{1/2}$ versus photon energy (hv) provides the band gap values (Fig. 4(b)) and found to be ~ 3.04 – 3.15 eV . Smaller band gap values compared to pure ZnO was due to the substitution of Nd³⁺ ions. Certain electronic states were offered into the band gap of ZnO by Nd³⁺ 4f electrons, which were situated close to the lower edge of the conduction band to form new lowest un-occupied molecular orbitals. The estimated values of E_g were tabulated in Table 2.

3.2. Morphological analysis

Schematic representations in Fig. 5 shows the formation of various ZnO: Nd³⁺ SS. The bio-surfactant with a suitable concentration can acquire different self-assembled SS (Kavyashree et al., 2015). Hence, in order to explore the above effect, several concentrations of *A.V.* (5–30 ml) on morphology were studied with a fixed 1 h sonication time. Fig. 6 shows the SEM images of the ZnO samples obtained at different *A.V.* concentration (5–30 ml). When the *A.V.* concentration was $\sim 5 \text{ ml}$ (Fig. 6a), irregular quasi-spherical petal built aggregates with rugged surfaces. When the *A.V.* concentration was $\sim 10 \text{ ml}$, the initial product largely contained of quasi-spherical particles with thick hierarchical platelets (Fig. 6b) and the obtained flower shaped structures were not well developed. When the *A.V.* concentration was $\sim 15 \text{ ml}$ (Fig. 6c), regular flower like spheres were formed and they were interconnected strongly. When the *A.V.* gel concentration was further increased to 20 ml (Fig. 6d), flower-like microspheres of thin nano plates were formed. When further increase in the *A.V.* concentration to 25 and 30 ml (Fig. 6(e and f)), there was no variations in the morphology except flowers like morphology. The large porous surfaces of these zinc oxide flowers found various applications in a display devices, catalysis, solar cells, sensors etc. The decrease in the aspect ratio of ZnO with an increase in the mass ratio of *A.V.* gel can be explained based on the interactions between the *A.V.* molecules and the surfaces of the growing crystals. At a low *A.V.* gel, the surfactant molecules interact more freely with each other and with the crystal surface. However, at a high *A.V.*, both the side facets and top facets of the crystals tend to adsorb ZnO molecules.

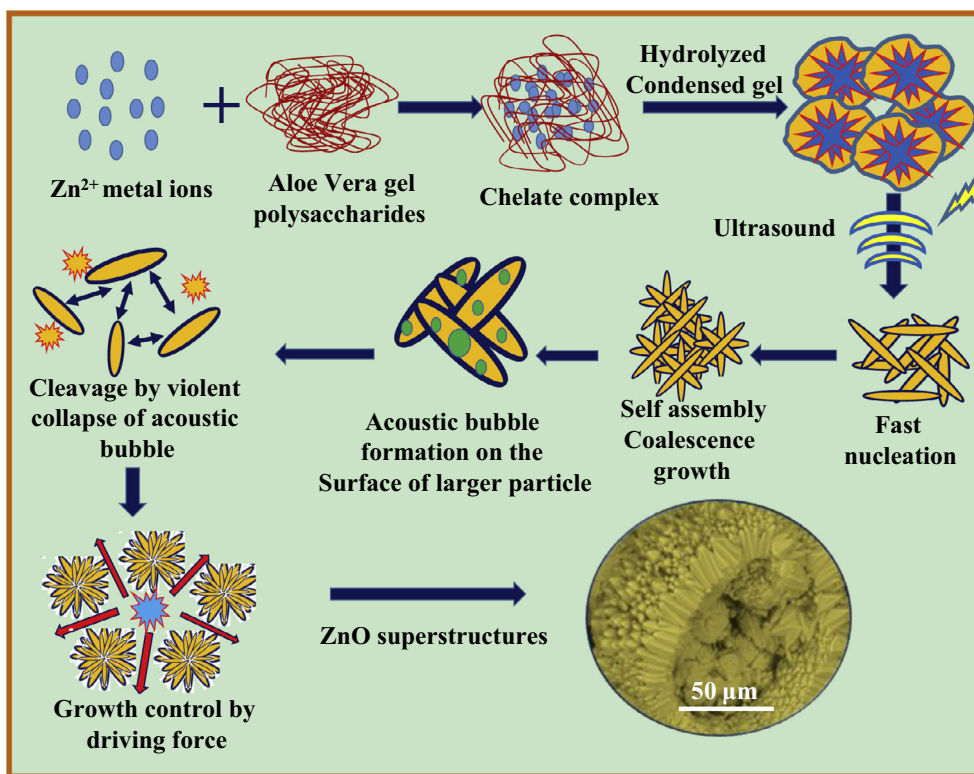


Fig. 5 Schematic representation for the formation of ZnO: Nd³⁺ SS.

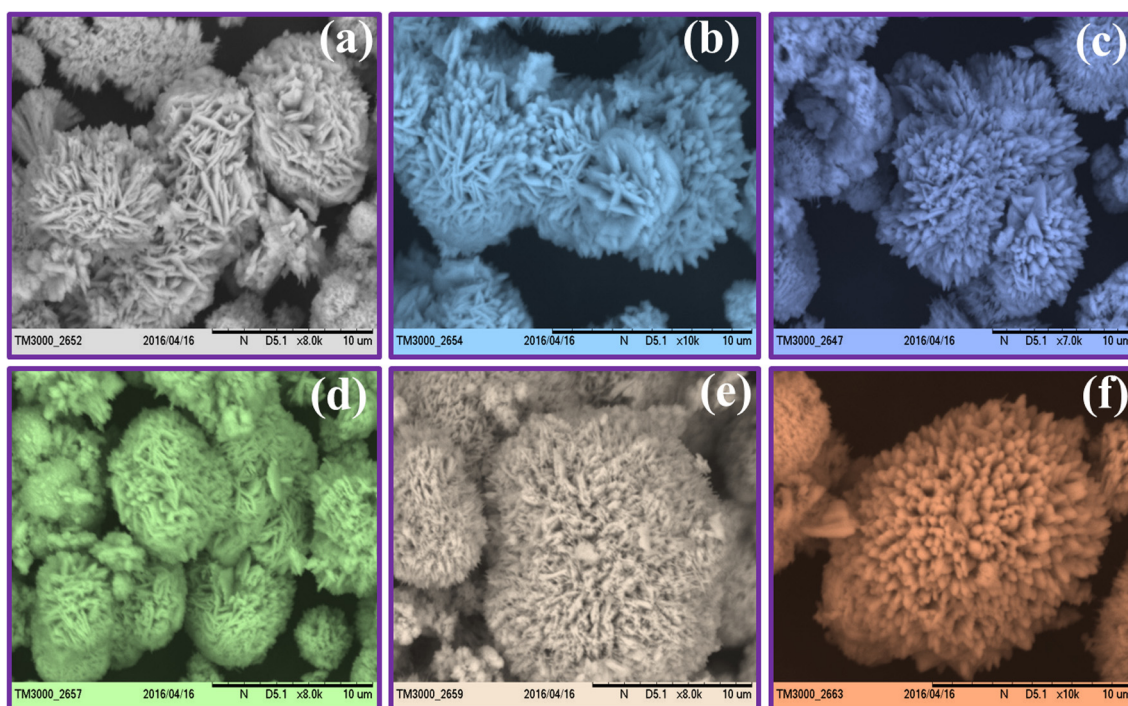


Fig. 6 SEM images of ZnO:Nd³⁺ (1 mol %) superstructures with different *A.V.* concentrations (a) 5 ml, (b) 10 ml, (c) 15 ml, (d) 20 ml, (e) 25 ml and (f) 30 ml.

The strong adsorption of the surfactants also blocks reactive sites to slow down the rate of addition of new element to the crystal facet and the supply of Zn²⁺ ions to the growing crystal

surface becomes more constrained. Since the crystal surface tends to be shielded by slow-growing and low-energy facets, the kinetic and thermodynamic aspects works in aggregation

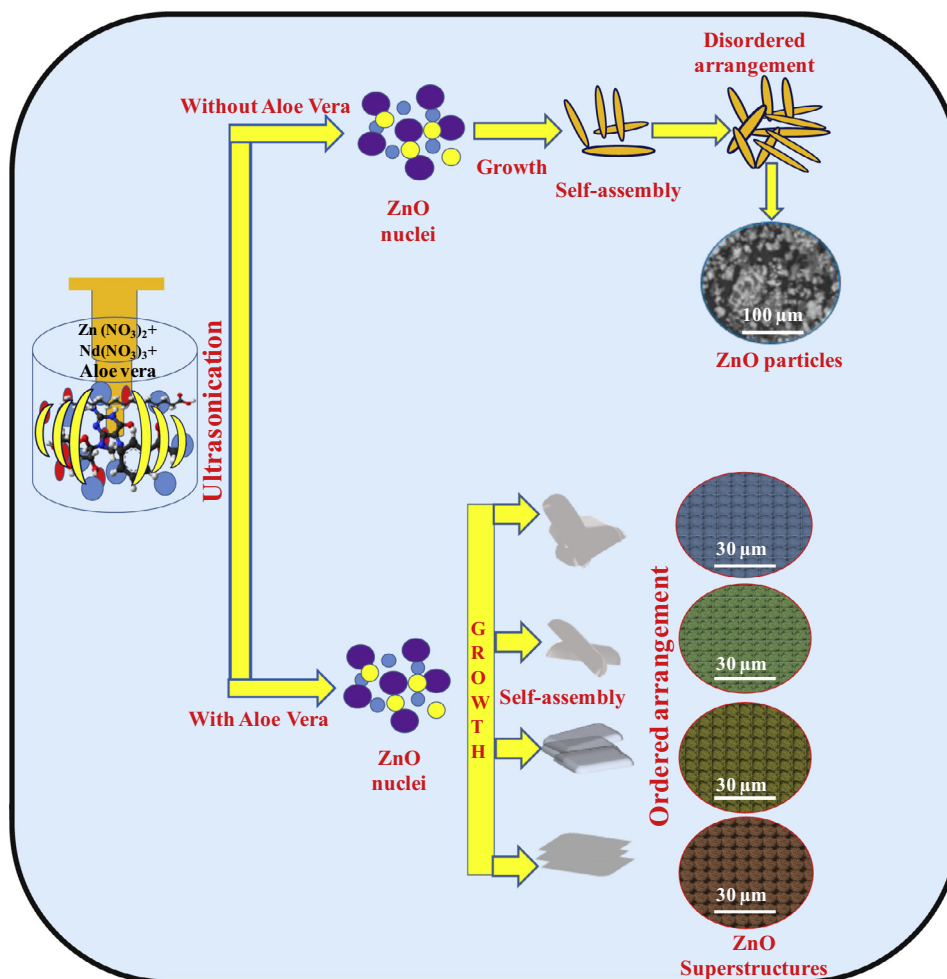


Fig. 7 Schematic representation of formation of ZnO:Nd³⁺ superstructures with and without *A.V.*

with one another. The changes in morphology can be observed with added *A.V.* specified that the bio-surfactants manipulate particle nucleation and growth. These outcomes were basically in line with the before findings that additives and surfactants modify the crystal growth stages and control nucleation. The growth rate of the crystal planes in ZnO was due to differences in the surface free energies leads to various crystal morphologies. Presence of many polysaccharides in the media can tune the shape during the growth of crystal and changes the crystal structures to undergo self-assembly (Lakshmeesha et al., 2014). The schematic representation for the formation of ZnO: Nd³⁺ SS with and without *A.V.* are shown in Fig. 7.

The various morphologies of the ZnO: Nd³⁺ (0.5–9 mol %) SS synthesized at different pH values with *A.V.* were as shown in Fig. 8. At a low pH of 1, the hexagonal rod shaped particles stacked side by side (Fig. 8(a)). With an increase of pH to 3, sharp hexagonal shaped particles assembled one over the other to form a single pyramid. However, when the pH is 5, a flower shaped with elongated tip to form bullet shaped particles (Fig. 8(c)). When the pH increases to 7, the obtained crystals were hexagonal with sharp tips which were self-assembled and projected outwards (Fig. 8(d)). However, with the increase of pH value to 9, hexagonal disc shaped SS were obtained (Fig. 8(e)). Therefore, it can be established that *A.V.* as a

bio-surfactant acts as a modifier to tune the structures. It seems plausible that bio-surfactant *A.V.* can absorb selectively on particular crystal facets or be integrated into the lattice leads to control over growth rate along different crystal axes to form various morphologies. It was observed that the pH may significantly impact the morphology of the material. In the growth stage, numerous tiny assembly units extend to grow into hierarchical SS and to decrease the surface energy. Numerous factors may influence to acquire SS, specifically crystal face attraction, electrostatic and dipolar fields associated with the aggregate, Vander Waals forces, intrinsic structures and external factors (Chandrashekar et al., 2015). The actual formation processes was more complicated and may require more studies.

SEM micrographs of ZnO: Nd³⁺ (5 mol %) SS with different sonication times (1–6 h) with 30 ml *A.V.* surfactant and ultrasonic power of 24 kHz, clearly evident that a various structural morphology were obtained (Fig. 9). For the crystallization of SS, two things can be considered: (i). Growth of nuclei and generation of the symmetrical form and (ii). Self-assembly of grown NPs and their orientation in different directions to form SS. It has been scientifically proven that the existence of SS is due to the possessing of more stability in symmetric shapes (Liu et al., 2015). Concerning to the

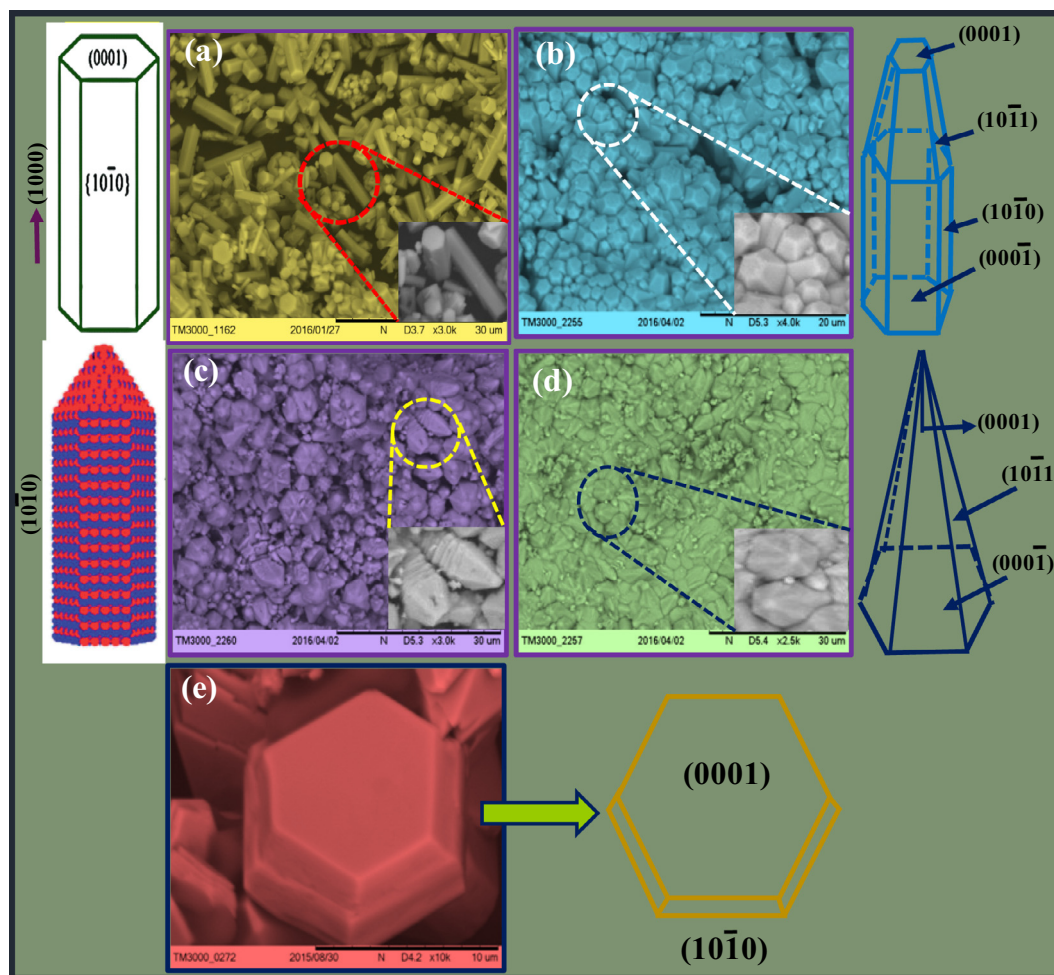


Fig. 8 SEM images of ZnO: Nd³⁺ superstructures at (a) pH = 1, (b) pH = 3, (c) pH = 5, (d) pH = 7 and (e) pH = 9.

tendency of having the symmetry and observation of the flower-like structure with the equal length branches, the first path seems more possible to happen. By this assumption, the probable mechanism for crystallization of the flower-like structure could be illustrated as follows: At first, the hexagonal prisms were considered as the primary nuclei of ZnO. The (0 0 1) face, which belongs to the symmetry group (C6) has higher symmetry and growth occurs along it (c-axis) (Sharifalhoseini et al., 2015).

It could be assumed that some primary nuclei (such as six nuclei) were joined. The samples produced under the high intensity irradiation, the aggregation or fusion of the ZnO nuclei was due to the transferring of the acoustic energy to the reaction medium. The impulsive collapse of the bubble generates localized hot spots through adiabatic compression or shock waves. Fusion of these nuclei could be exemplified by the high temperature and high pressure produced in the hot spots.

The mechanism of formation of ZnO nanostructures takes the consideration of the ionic species formed from water molecules by absorption of ultrasound energy. The reaction steps taking place inside sonochemical bath can be summarized in

Fig. 10. Equations written inside the Fig. 10 were the possible reactions for the formation of primary ions by dissociation of water, sodium hydroxide and zinc acetate. Fourth equation in the inset of Fig. 10 shows the formation of [Zn(OH)₄]²⁻ species which further decomposes to give ZnO SS.

When zinc nitrate mixed with *A.V.* plant gel, the Zn²⁺ ions will distribute uniformly, thus forming a three-dimensional polymeric network structure. The resulting polymeric network undergoes slow decomposition when subjected to ultrasonic irradiation. The detailed study was necessary to understand the formation of different ZnO: Nd³⁺ SS. The complexity and variety of polysaccharides can be explained by two ways, first monosaccharides can be linked together in different ways (1 to 2, 1 to 3, 1 to 4, 1 to 5 and 1 to 6 in an α and β configurations) and second due to the presence of branched chains (Ray et al., 2015). During the process, pectin and acemannan serve as bio templates to restrict the growth of ZnO structures, but also serve as assembling agents to get SS. Similarly cellulose, hemicelluloses, chitosan, xylan, etc. also contribute in stabilization of Nd³⁺ ions to obtain various morphologies. The nature prefers the least utilization of energy in any of the self-assemblies. Hence in this method of preparation for the

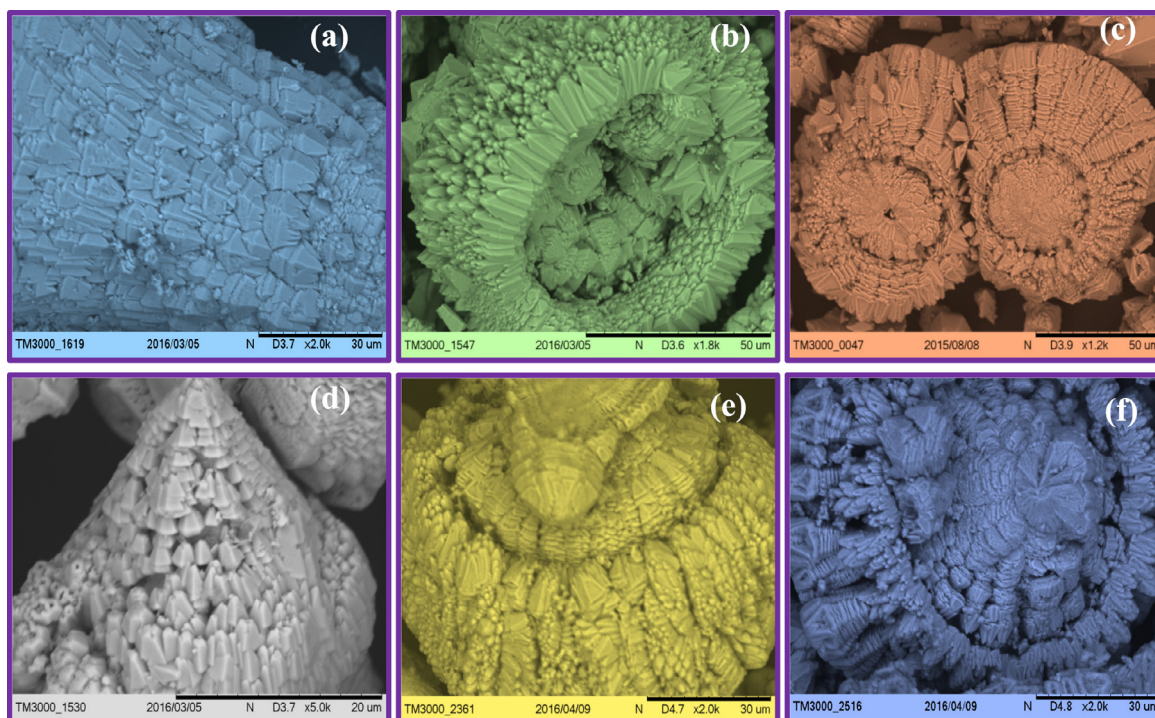


Fig. 9 SEM images of ZnO: Nd³⁺ superstructures with different sonication time (a) 1 h, (b) 2 h, (c) 3 h, (d) 4 h, (e) 5 h (f) 6 h with 30 ml *A.V.* and 24 kHz ultrasonic power.

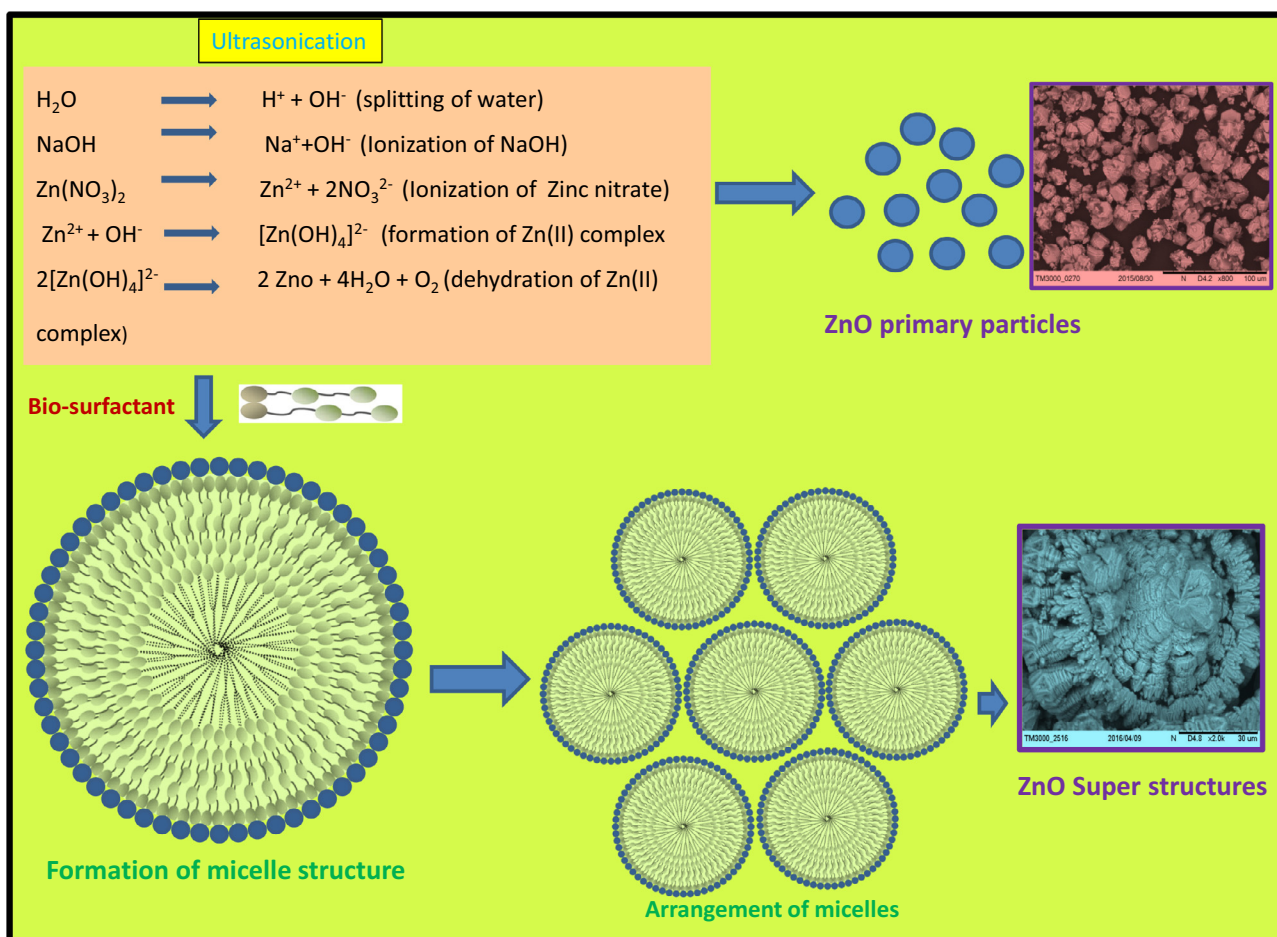


Fig. 10 Mechanism showing growth, arrangement of micelle resulting to ZnO:Nd³⁺ superstructures.

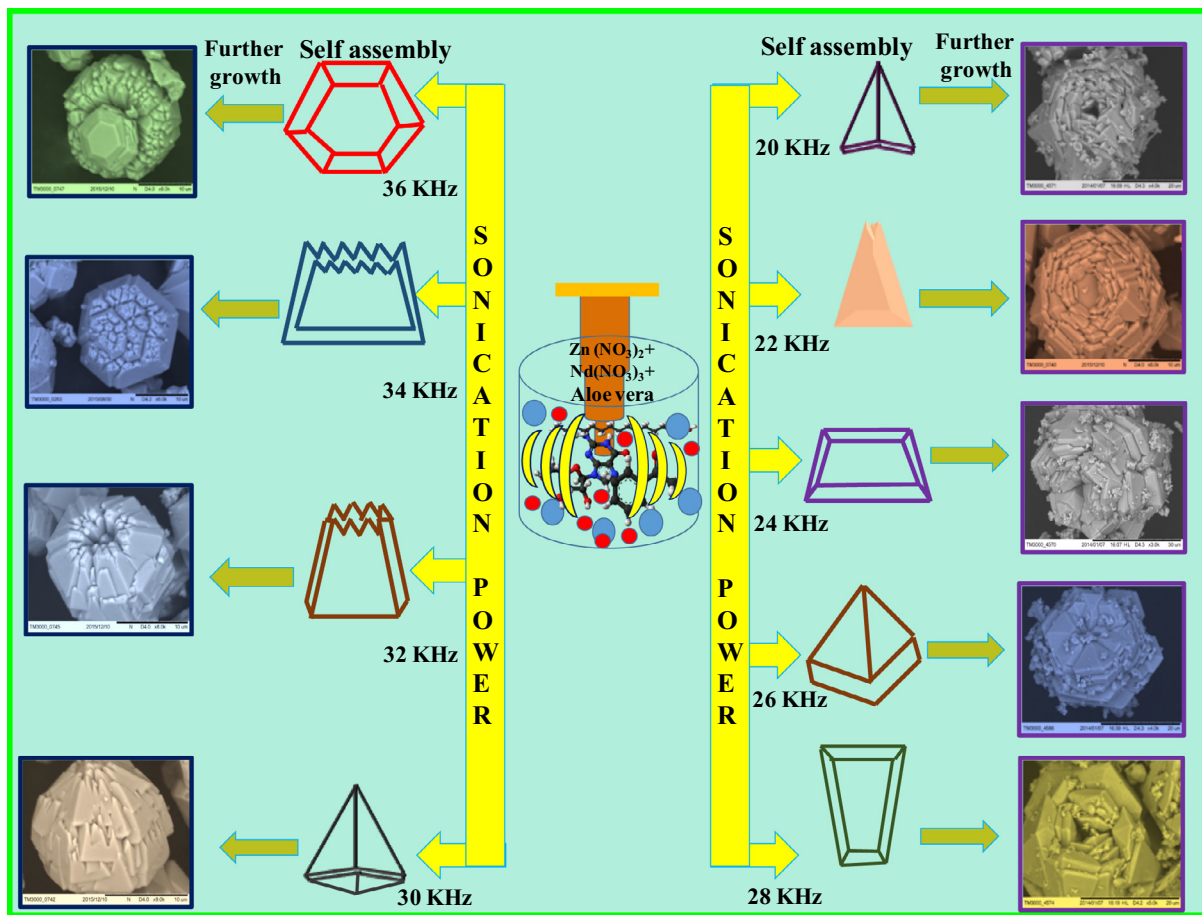


Fig. 11 SEM images of ZnO: Nd³⁺ superstructures synthesized at various ultrasonic power (20–36 kHz).

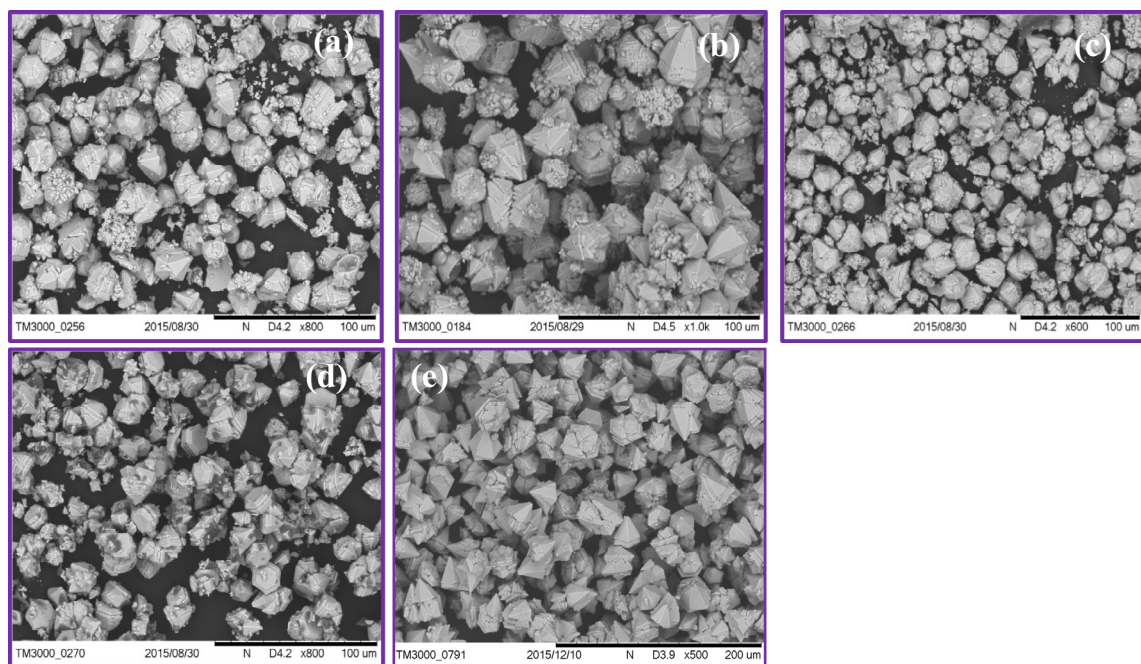


Fig. 12 Formation of cone-like structures of ZnO: Nd³⁺ with 30 ml of *A.V.* and 24 kHz ultrasonication power at different temperatures (a) 313 K (b) 323 K (c) 233 K (d) 343 K (e).

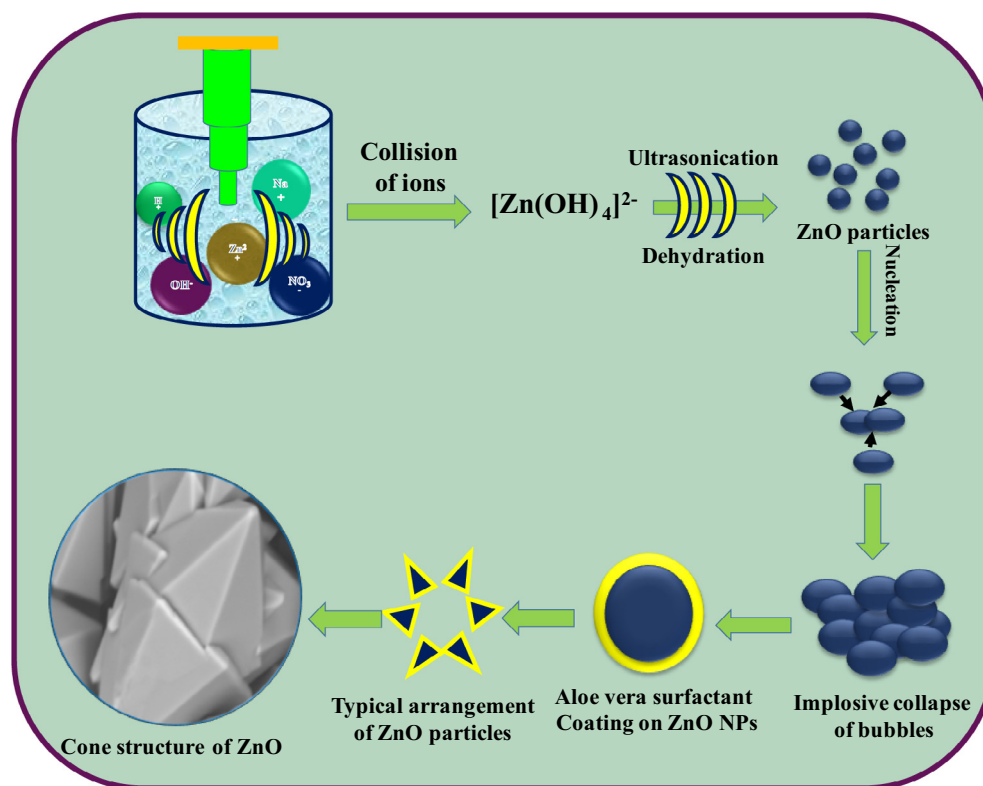


Fig. 13 Schematic illustration of formation of Cone-like structures of ZnO:Nd³⁺ at different temperatures.

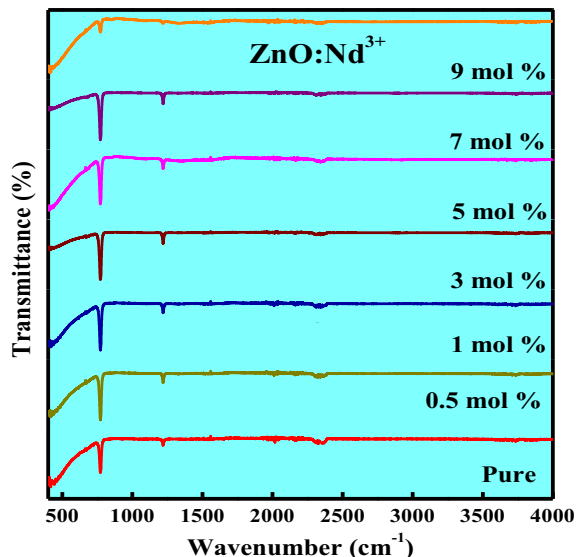


Fig. 14 FTIR spectra of ZnO: Nd³⁺ (0.5–9 mol %) NPs.

formation of SS of ZnO was due to the nature's least energy utilization concepts.

Fig. 11 shows the SEM images of ZnO: Nd³⁺ SS synthesized at various ultrasonic powers (20–36 kHz). It was noticed that by changing the sonication power may significantly influence the hexagonal pyramidal shape morphology of the product. By changing the suitable sonication power, the shape of

the SS could prominently alter. In the growth stage, many of the tiny pyramidal assembly units extend to grow into hierarchical flower SS to reduce the surface energy. Numerous factors which may influence to achieve the flower like SS, includes crystal- face attraction, electrostatic and dipolar fields associated with the aggregate, Vander Waals forces, intrinsic structures and external factors. In order to find out the possibility for the formation of ZnO SS as a function of temperature a sonochemical reaction was performed in the temperature range of 313–343 K.

It was interesting to note that pyramidal like structure with several solid agglomerates (irregular) instead of well-crystallized NPs were formed at 313–343 K (Fig. 12(a–d)). However, when the temperature increased to 343 K a smooth hexagonal uniform pyramidal shaped particles were obtained (Fig. 12(e)) which indicates that temperature was an indispensable factor to determine the formation of well-crystallized hexagonal uniform pyramidal shaped particles. The schematic illustration for the formation of cone-like structures at different temperatures was shown in Fig. 13.

Fig. 14 shows the FTIR spectra of pure and Nd³⁺ (0.5–9 mol %) doped ZnO NPs. The spectra exhibit significant absorption bands at 3748, 1218 and 772 cm⁻¹ are due to O–H stretching, H–O–H bending vibrational modes due to the adsorption of moisture and Zn–O stretching vibrations respectively. Fig. 15 shows the TEM and HRTEM images of ZnO: Nd³⁺ (1 mol %) NPs. TEM images show that the particles were in nano size in the range 45–60 nm. The HRTEM images shows the polycrystalline nature with interplanar spacing of about 0.26–0.32 nm (Fig. 15(b)).

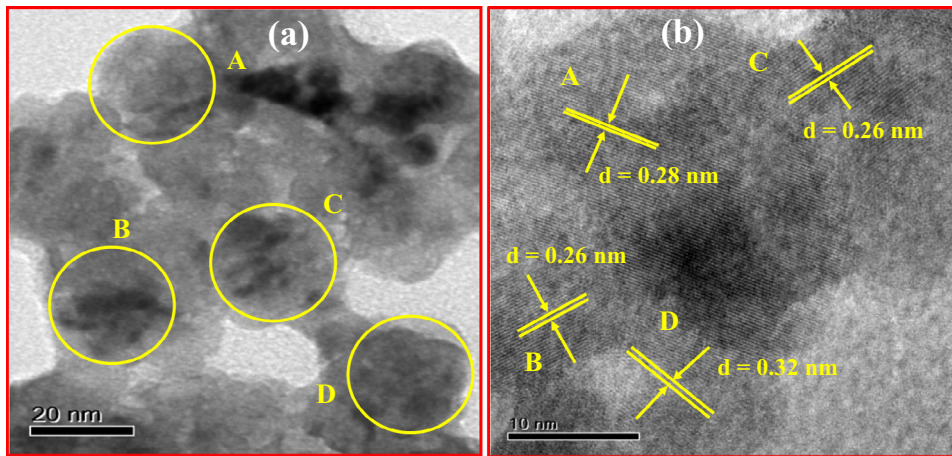


Fig. 15 (a) TEM and (b) HRTEM of ZnO: Nd³⁺ (1 mol %) NPs.

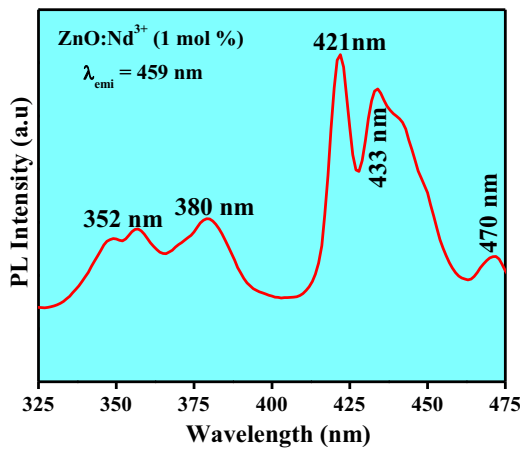


Fig. 16 Excitation spectrum of ZnO:Nd³⁺ (1 mol %) NPs.

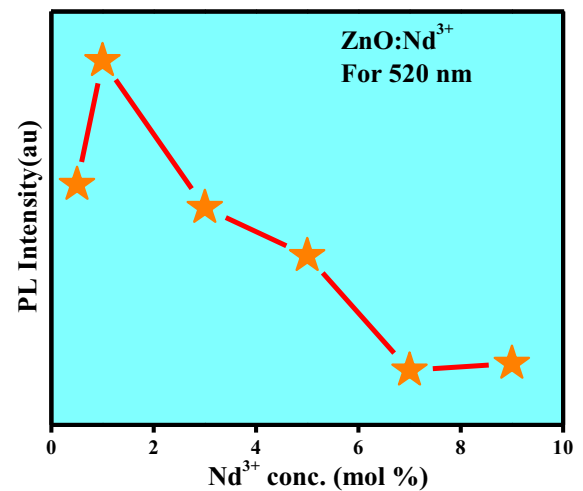


Fig. 18 Variation PL intensity with concentration of Nd³⁺ (0.5–9 mol %) in ZnO NPs.

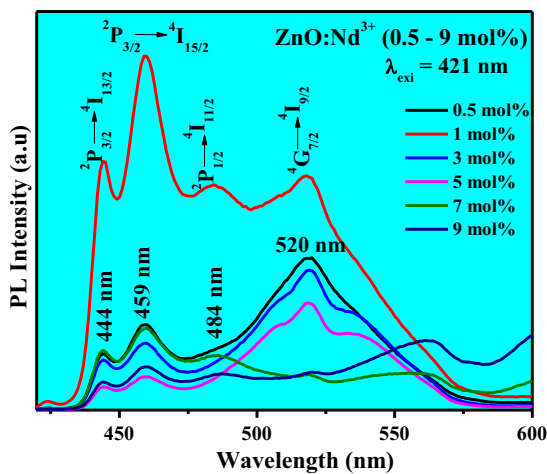


Fig. 17 Emission spectra of ZnO:Nd³⁺ (0.5–9 mol %) NPs excited at 421 nm.

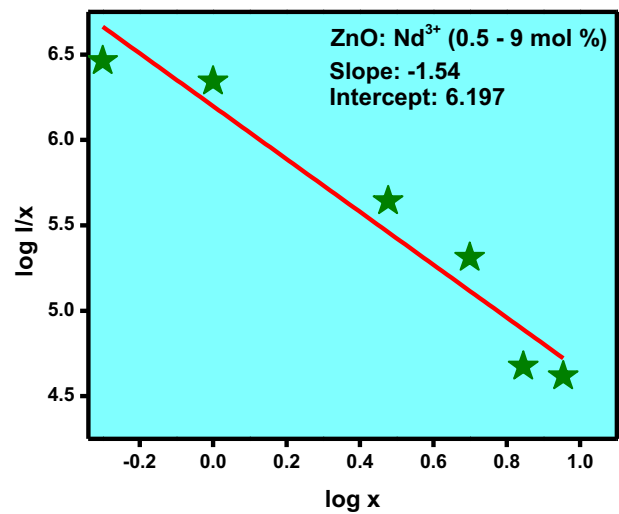
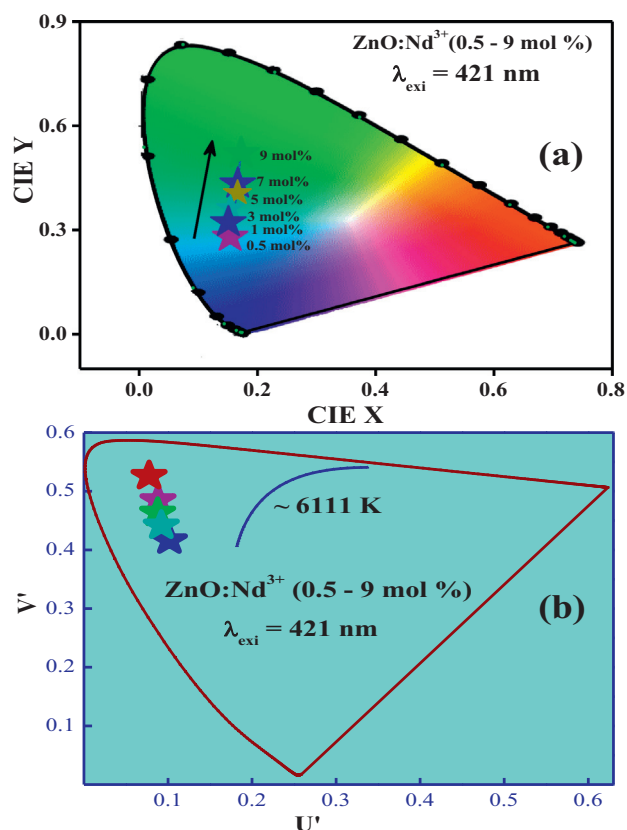


Fig. 19 Relation between $\log(x)$ and $\log(I/x)$ in ZnO: Nd³⁺ (0.5–9 mol %) NPs.

Table 4 Photometric characteristics of Nd³⁺ (0.5–9 mol %) doped ZnO NPs.

Nd ³⁺ (mol %)	CIE		CCT		CCT (K)	CRI (%)
	X	Y	U'	V'		
0.5	0.1668	0.4336	0.0847	0.4958	7800	88.13
1	0.1539	0.2801	0.1016	0.4165	7161	90.12
3	0.1664	0.4064	0.0882	0.4848	6855	91.00
5	0.1726	0.5205	0.0775	0.5263	6632	92.48
7	0.1546	0.3630	0.0877	0.4636	7394	93.16
9	0.1510	0.3221	0.0920	0.4417	6937	94.78

**Fig. 20** (a) CIE, (b) CCT diagram of ZnO:Nd³⁺ (0.5–9 mol %) NPs.

3.3. Photoluminescence (PL) properties

The PL spectra inform surface defects, oxygen vacancies, photo induced charge carrier separation and recombination processes in nano sized semiconductor materials (Kolesnikov et al., 2015). Excitation spectra of the ZnO: Nd³⁺ NPs under λ_{emi} is equal to 459 nm (Fig. 16). Charge transfer band could be estimated using the following equation given by Jørgensen as reported elsewhere (Chen et al., 2015). For $\chi(\text{Zn}^{2+}) = 1.65$ and $\chi(\text{Nd}^{3+}) = 1.14$, the calculated CT position should be $15,300 \text{ cm}^{-1}$, the measured positions of CT bands in the excitation spectra of obtained samples were at around 653 nm. But in the present case no CT band was observed. This uncommon phenomenon indicates that no efficient radiative energy transfer occurs between activator and host. PL emission

spectra of ZnO: Nd³⁺ (0.5–9 mol %) phosphor excited by 421 nm at RT was shown in Fig. 17. The spectra exhibits strong near ultraviolet emission peaks at 444, 459, 484 nm and broad green emission centered at about 520 nm which corresponds to $^2\text{P}_{3/2} \rightarrow ^4\text{I}_{13/2}$, $^2\text{P}_{3/2} \rightarrow ^4\text{I}_{15/2}$, $^2\text{P}_{1/2} \rightarrow ^4\text{I}_{11/2}$ and $^4\text{G}_{7/2} \rightarrow ^4\text{I}_{9/2}$ transitions, respectively and these were the emission bands were the characteristic peaks of Nd³⁺. The near ultraviolet emission results from exciton recombination corresponds to the near edge emission of ZnO. The ultraviolet emission was closely connected with the density of free exciton in ZnO phosphor. Variations of PL intensities with respect to Nd³⁺ concentration were as shown in Fig. 18. The PL intensity increases up to 1 mol % and after that it diminishes due to the concentration quenching. Addition of 1 mol % of Nd³⁺ in ZnO, the crystalline quality increases leads to increase in the density of free excitons. The similar results were also observed in Mg and Al doped ZnO nanostructures (Giri and Chakrabarti, 2016). At higher concentration, the distance between the activator Nd³⁺ ions decreases which leads to the non-radioactive energy transfer among Nd³⁺ ions. In this context, the critical distance (R_c) was estimated and found to be $\sim 2.99 \text{ \AA}$ (Ramakrishna et al., 2016a,b). For Nd³⁺ ions, calculated value of R_c was less than 5 \AA leads to the multipole–multipole interaction in the ZnO host. From Dexter and Schulman (Vinod et al., 2014; Venkataravanappa et al., 2016) statements, multi- polar interaction intensity can be resolved based on the change in the emission intensity from the emitting level that has multipolar interaction. The curve of $\log I/\chi$ v/s. $\log \chi$ in ZnO: Nd³⁺ phosphor was shown in Fig. 19 and which clearly shows that the relation is approximately linear and the value of slope was ~ -1.54 . The calculated value Q was found to be 4.62 is almost equal to 5. This result indicates that the charge transfer mechanism was due to $d-d$ interaction for the concentration quenching transition of ZnO: Nd³⁺ NPs.

The quantum efficiency (Q_E) of ZnO: Nd³⁺ (5 mol %) is estimated by the relation

$$Q_E = \frac{E_C - E_a}{L_a - L_c} \quad (1)$$

where E_C ; integrated lumen of the phosphor caused by direct excitation, E_a ; integrated lumen from the empty integer along sphere (without sample), L_a ; excitation profile from the empty integrating sphere and L_c ; Integrated excitation profile when the phosphor was directly emitted by incident beam. The Q_E of the specified phosphor was found to be $\sim 68.14\%$.

The estimate CIE values using PL spectra were tabulated in Table 4. From Fig. 20(a) it was observed that the position of the colour coordinates were tuned from blue to pale green

Table 5 Antibacterial activity of ZnO: Nd³⁺ (1 mol %) doped NPs synthesized using different volume of *Aloe vera* extract against Gram-positive *Staphylococcus aureus*, Gram-negative, *Pseudomonas aeruginosa*, *Klebsiella pneumoniae* and *Escherichia coli* (Concentration expressed as µg/mL).

Organism					
Nd ³⁺ Conc. (mol %)		<i>K. pneumoniae</i>	<i>S. aureus</i>	<i>P. aeruginosa</i>	<i>E. coli</i>
ZnO Pure	MIC	0.25	2.5	2.5	2.5
	MBC	2.5	25	25	25
0.5	MIC	0.025	0.0025	0.25	2.5
	MBC	0.25	0.025	2.5	25
1	MIC	0.0025	0.0025	0.025	0.25
	MBC	0.025	0.025	0.25	2.5
3	MIC	0.025	0.25	0.25	0.25
	MBC	0.25	2.5	2.5	2.5
5	MIC	0.25	2.5	0.25	2.5
	MBC	2.5	25	2.5	25
7	MIC	2.5	0.025	2.5	2.5
	MBC	25	0.25	25	25
9	MIC	0.25	0.25	0.25	0.025
	MBC	2.5	2.5	2.5	0.25

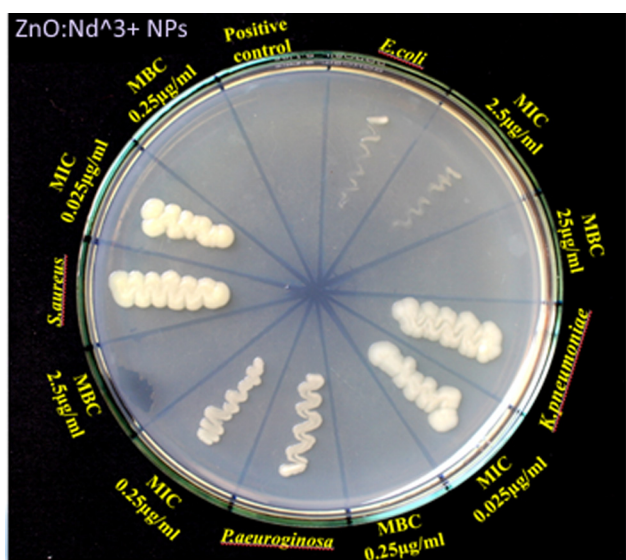


Fig. 21 MIC and MBC values of ZnO: Nd³⁺ NPs synthesized using *Aloe vera* (1 ml).

region by increasing the concentration of Nd³⁺ ions as a dopant (Schanda and Danyi, 1977). The CCT was estimated and by determining the temperature of the closest point of the Planckian locus to the light source on the (U₀, V₀) uniform chromaticity diagram (Fig. 20(b)).

Also, the quality of white light in terms of colour correlated temperature (CCT) was given by McCamy empirical formula $CCT = -437m^3 + 3601m^2 - 6861m + 5514.31$ (theoretical) where $m = (x - x_c)/(y - y_c)$; the inverse slope line and chromaticity epicenter was at $x_c = 0.3320$ and $y_c = 0.1858$ (Ramakrishna et al., 2016a,b). Generally, a CCT value greater than 5000 K indicates the cold white light used for commercial lighting purpose. The obtained CCT value (6111 K) for the near white light emitting phosphor agrees with the CCT value of standard daylight at noon (D65, 6500 K) suitable for cold

near white light emission. Calculated values of CCT for each sample was summarized in Table 4 and were in acceptable range and can be considered “warm” in appearance. Any NPs can be distinguished by their dominant wavelength and colour purity. The colour rendering index (CRI) values (Table 4) varied very close to 93.38% indicates that the prepared phosphor materials may be excellent materials for WLED applications.

3.4. Antibacterial assay of ZnO-Nd³⁺ NPs

The present investigation focuses on pathogenic bacteria that were noteworthy medical implications. These pathogenic microorganisms were accountable for numerous diseases, cases of hospital infection, colonization of medical devices and also reported for the ability to acquire resistance (Sanchez et al., 2013; Toledo et al., 2012). MIC and MBC values of all the synthesized samples against bacteria were shown in Table 5 and Fig. 21. ZnO: Nd³⁺ NPs showed significant inhibition against *E. coli*, *K. pneumoniae*, *P. aeruginosa* and *S. Aureus* with discrete differences in the susceptibility to ZnO-Nd NPs in a dose-dependent manner. The MICs observed for the Gram-positive bacteria, *Staphylococcus aureus* with 0.0025 µg/mL (Table 5). For the Gram-negatives, ZnO-Nd NPs presented a MIC 0.025 µg/mL for *E. coli*, 0.0025 µg/mL for *K. pneumoniae* (the lowest observed in the Gram-negative bacteria) and 0.025 µg/mL for *P. aeruginosa* with NPs prepared with *A.V.* (1 ml), it also presents a higher potency compared to all other conditions (Table 5).

In relation to MBC test, *K. pneumoniae* again showed a higher susceptibility to ZnO-Nd NPs (0.025 µg/mL) than to *E. coli* (0.25) and *P. aeruginosa* with 0.25 µg/mL and to *Staphylococcus aureus* with 0.025 µg/mL with NPs prepared with *A.V.* (1 ml) and it was showed identical results to the MIC test for both the agents. However, NPs prepared with different volume of extract were having higher than the above mentioned concentrations (Table 5). This outstanding antibacterial activity of ZnO: Nd³⁺ NPs was due to the high surface area to

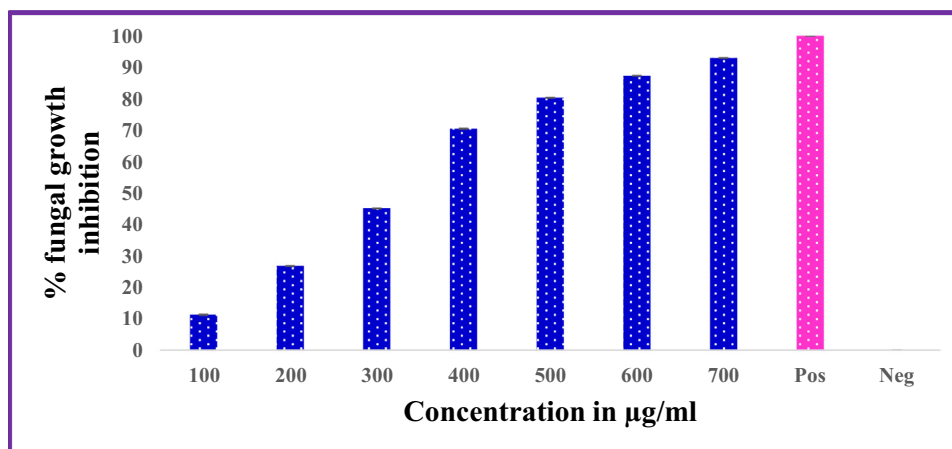


Fig. 22 Inhibitory effect of ZnO Nd³⁺ NPs against *Alternaria alternata*.

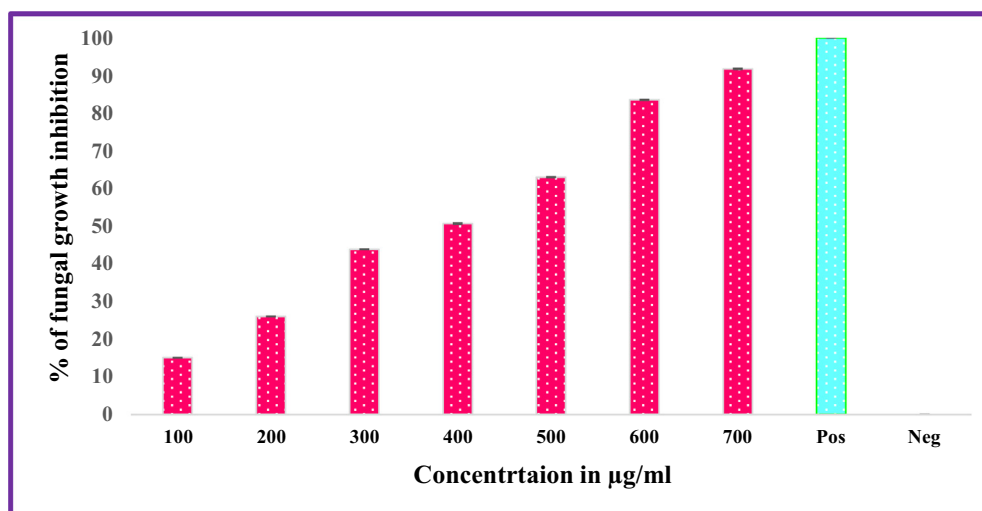


Fig. 23 Inhibitory effect of ZnO:Nd³⁺ NPs against *Fusarium oxysporum*.

volume ratio of NPs and reactive oxygen species production (Navale et al., 2015).

3.5. Antifungal activity of ZnO-Nd NPs

ZnO-Nd NPs showed the inhibitory effect on the growth of *Alternaria alternata* and *Fusarium oxysporum* that were cultured on SDA containing different concentrations of ZnO: Nd³⁺ NPs (100, 200, 300, 400, 500, 600 and 7000 µg/mL) incubated at 298 K for 7 days (Figs. 22–24). Commonly, the use of ZnO: Nd³⁺ NPs suspension was effective in inhibiting fungal growth for both *Alternaria alternata* and *Fusarium oxysporum*. The average growth of *Alternaria alternata* was inhibited by from 91.77% in terms of colony growth diameters after 7 days of incubation as the concentration of ZnO: Nd³⁺ NPs increased from 100 to 700 µg/mL with a near complete inhibition at 700 µg/mL (Table 6). For *Fusarium oxysporum*, the reduction rate of fungal growth varied from 92.95% as the concentration of ZnO-Nd NPs increased from 100 to 700 µg/mL with a near complete inhibition at 700 µg/mL. Significant

difference was found for different concentrations of ZnO: Nd³⁺ NPs treatment ($P < 0.05$). These results indicate that ZnO: Nd³⁺ NPs at concentration greater than 700 µg/mL can significantly inhibit the growth of the fungi, *Alternaria alternata* and *Fusarium oxysporum*.

4. Conclusions

ZnO: Nd³⁺ (0.5–9 mol %) NPs prepared by bio-surfactant assisted ultrasound method. The growth mechanism for various SS formation was proposed with egg box concept. The use of *A.V.* helped in tuning the morphology of ZnO:Nd³⁺ samples due to the preferential adsorption of polysaccharides, resulted in a hexagonal like shapes. In addition, improved crystallization with less process time and energy consumptions was observed when compared to the other conventional techniques. Photometric properties of prepared NPs by ultrasound route can be highly useful for display and solid state lightning applications. Nanobactericides and nanofungicides can be obtained in a cost-effective manner and are suitable for



Fig. 24 Antifungal activity of ZnO:Nd³⁺ NPs against Plant pathogenic fungi *Alternaria alternata* and *Fusarium oxysporum*.

Table 6 Percentage of inhibition by ZnO: Nd³⁺ (1 mol %) NPs against *Fusarium oxysporum* and *Alternaria alternata*.

Concentration in µg/ml (ZnO Nd)	<i>Fusarium oxysporum</i>	<i>Alternaria alternata</i>
100	11.26 ± 0.1154	15.06 ± 0.0333
200	26.76 ± 0.0577	26.02 ± 0.0577
300	45.07 ± 0.0667	43.83 ± 0.0577
400	70.42 ± 0.0577	50.68 ± 0.1201
500	80.28 ± 0.0577	63.01 ± 0.1201
600	87.38 ± 0.0577	83.56 ± 0.1201
700	92.95 ± 0.0577	91.778 ± 0.1154
Positive control	100	100
Negative control	0	0

articulating new categories of nanoantibiotics. These constituents would be used as an innovative, ecofriendly, antimicrobial for diverse bacterial and mycopathogenic organisms

of humans and plants. ZnO:Nd³⁺ NPs prepared using *A.V.* gel of 1 ml showed better antibacterial and antifungal activities against the selected well known pathogenic bacteria and fungi.

Acknowledgement

The author Dr. H Nagabhushana thanks to DST Nano Mission New Delhi for the sanction of this Project.

We deeply acknowledge the contributions of our co-author Late Dr. M. K. Sateesh. Let his soul rest in peace in the feet of almighty.

References

- Albiss, B.A., Al-Widyan, M.I., Obaidat, I., 2016. *Ceram. Int.* 42, 3563–3568.
- Ali, N., Hussain, A., Ahmed, R., Wang, M.K., Zhao, C., UlHaq, B., Fu, Y.Q., 2016. *Renew. Sustainable Energy Rev.* 59, 726–737.
- Amutha, C., Thanikaikarasan, S., Ramadas, V., Asath Bahadur, S., Natarajan, B., Kalyani, R., 2016. *Optik* 127, 4281–4286.
- Ambika, S., Sundrarajan, M., 2015. *J. Photochem. Photobiol., B* 149, 143–148.
- Basavaraj, R.B., Nagabhushana, H., Daruka Prasad, B., Sharma, S. C., Prashantha, S.C., Nagabhushana, B.M., 2015. *Optik*. 126, 1745–1756.
- Bhattacharyya, S., Gedanken, A., 2008. *Micropor Mesopor Mat.* 110, 553–559.
- Bouazizi, N., Ajala, F., Bettaibi, A., Khelil, M., Benghnia, A., Bargougui, R., Louhichi, S., Chandrashekar, L., Nagabhushana, M.H., Vidya, Y.S., Anantharaju, K.S., Sharma, S.C., Premkumar, H.B., Prashantha, S.C., Daruka Prasad, B., Shivakumara, C., Saraf, Rohit, Nagaswarupa, H.P., 2015. *J. Mol. Catal. A Chem.* 409, 26–41.
- Chandrashekar, M., Nagabhushana, H., Vidya, Y.S., Anantharaju, K. S., Sharma, S.C., Premkumar, H.B., Prashantha, S.C., Daruka Prasad, B., Shivakumara, C., Saraf, Rohit, Nagaswarupa, H.P., 2015. *J. Mol. Catal. A Chem.* 409, 26–41.
- Chawla, S., Rawal, R., Kumar, D., Pundir, C.S., 2012. *Anal. Biochem.* 430, 16–23.
- Chen, W., Hou, Yi, Osvet, Andres, Guo, Fei, Kubis, Peter, Batentschuk, Mirosław, Winter, Benjamin, Spiecker, Erdmann, Forberich, Karen, Brabec, Christoph J., 2015. *Org. Electron.* 19, 113–119.
- Cheng, Y., Tang, F., Xue, H., Liu, H., Gao, B., Feng, Y., 2016. *Mater Sci. Semicond. Process.* 45, 9–16.
- Duo, S., Li, Y., Zhang, H., Liu, T., Wu, K., Li, Z., 2016. *Mater Charact.* 114, 185–196.
- Eskandarloo, H., Badii, A., Behnajady, M.A., Ziarani, G.M., 2016. *Ultrason. Sonochem.* 28, 169–177.
- Ghandomani, S.K., Yousefi, R., Jamli-Sheini, F., Huang, N.M., 2014. *Ceram. Int.* 40, 7957–7963.
- Giri, P., Chakrabarti, P., 2016. *Superlattices Microstruct.* 93, 248–260.
- Guilera, J., Cristian, F., Olga, C., Francisco, H.R., Shuangzhou, W., Sanjay, M., Florian, U., Andrea, D.L., Zeeshan, A., Albert, R., Daniel, P.J., Joan, R.M., 2016. *Sensor Actuat B-Chem.* 221, 104–112.
- Jain, R., Dhanjai, Sinha, A., 2016. *Appl. Surf. Sci.* 369, 151–158.
- Ji, P., Zhang, Y., 2016. *Phys. Lett. A.* 380, 1551–1555.
- Khataee, A., Karimi, A., Arefi-Oskoui, S., Darvishi, R., Soltani, C., Hanifehpour, Y., Soltani, B., Joo, S.W., 2015a. *Ultrason. Sonochem.* 22, 371–381.
- Khataee, A., Soltani, R.D.C., Karimi, A., Joo, S.W., 2015b. *Ultrason. Sonochem.* 23, 219–230.
- Khataee, A., Saadi, S., Safarpour, M., Joo, S.W., 2015c. *Ultrason. Sonochem.* 27, 379–388.

- Khataee, A., Vahid, B., Saadi, S., Joo, S.W., 2016. *Ultrason. Sonochem.* 29, 146–155.
- Kavyashree, D., Shilpa, C.J., Nagabhushana, H., Daruka Prasad, B., Sreelatha, G.L., Sharma, S.C., Ashoka, S., Anandakumari, R., Premkumar, H.B., 2015. *ACS Sustainable Chem. Eng.* 6, 1066–1080.
- Kolesnikov, I.E., Tolstikova, D.V., Kurochkin, A.V., Platonova, N. V., Pulkin, S.A., Manshina, A.A., Mikhailov, M.D., 2015. *Mater. Res. Bull.* 70, 799–803.
- Lakshmeesha, T.R., Sateesh, M.K., Daruka Prasad, B., Sharma, S.C., Kavyashree, D., Chandrasekhar, M., Nagabhushana, H., 2014. *Cryst. Growth Des.* 14, 4068–4079.
- Liu, X., Huang, Wenyi, Cheng, Hao, Huang, Bangbiao, Bai, Dawei, Fu, Fengming, Wu, Hongda, Li Lijun, 2015. *Appl. Surf. Sci.* 356, 240–248.
- Ma, X., Luo, Wen, Yan, Mengyu, He, Liang, Mai, Liqiang, 2016. *Nano Energy.* 24, 165–188.
- Madan, H.R., Sharma, S.C., Udayabhanu, Suresh, D., Vidya, Y.S., Nagabhushana, H., Rajanaik, H., Anantharaju, K.S., Prashantha, S.C., Maiya, P.S., 2016. *Spectrochim. Acta, Part A.* 152, 404–416.
- Meshram, S.P., Adhyapakn, P.V., Amalnerkar, D.P., Mulla, I.S., 2016. *Ceram. Int.* 42, 7482–7489.
- Morozov, I.G., Belousova, O.V., Ortega, D., Mafina, M.K., Kuznetsov, M.V., 2015. *J. Alloys Compd.* 633, 237–245.
- Moussa, H., Girot, E., Mozet, K., Alem, H., Medjahdi, G., Schneider, R., 2016. *Appl Catal B-Environ.* 185, 11–21.
- Mucur, S.P., Tumay, T.A., Birdogan, S., San, S.E., Tekin, E., 2015. *Nano-Struct. Nano-Objects.* 1, 7–14.
- Nagabhushana, H., Basavaraj, R.B., Daruka Prasad, B., Sharma, S. C., Premkumar, H.B., Udayabhanu, Vijayakumar, G.R., 2016. *J. Alloys Compd.* 669, 232–239.
- Navale, G.R., Thripuranthaka, M., Late, D.J., Shinde, S.S., 2015. *J. Sci Med .Nanotechnol. Nanomed.* 3, 2–9.
- Nithya, A., Krupa, D., Vimala, R., 2016. *Mater. Sci. Eng., C* 61, 728–735.
- Pachauri, V., Kern, K., Balasubramanian, K., 2010. *Chem. Phys. Lett.* 498, 317–322.
- Peng, F., Liu, Wenpeng, Zhang, Qingli, Yang, Huajun, Shi, Chaoshu, Mao, Rihua, Sun, Dunlu, Luo, Jianqiao, Sun, Guihua, 2014. *J. Crys. Gro.* 406, 31–42.
- Peng, Y., Ji, J., Chenc, D., 2015. *Appl Surf Sci.* 356, 762–768.
- Ramakrishna, G., Nagabhushana, H., Basavaraj, R.B., Prashantha, S. C., Sharma, S.C., Naik, Ramachandra, Anantharaju, K.S., 2016a. *Optik.* 127, 5310–5315.
- Ramakrishna, G., Naik, Ramachandra, Nagabhushana, H., Basavaraj, R.B., Prashantha, S.C., Sharma, S.C., Anantharaju, K.S., 2016b. *Optik.* 127, 2939–2945.
- Ramanujam, J., Amit, V., 2016. *Prog. Mater. Sci.* 82, 294–404.
- Ramesh, M., Anubavam, M., Viruthagiri, G., 2015. *Spectrochim. Acta Part A.* 136, 864–870.
- Ray, A., Ghosh, Sampad, Ray, Arjun, Aswatha, Shashaank M., 2015. *Ind. Crops. Prod.* 76, 298–305.
- Sanchez, G.V., Master, R.N., Clark, R.B., Fyyaz, M., Duvvuri, P., Ekta, G., Bordon, J., 2013. *Emerg. Infect. Dis.* 19, 133–136.
- Sara, A., Jadwisieniczak, W.M., Wright, J.T., David, P., Faiz, R., 2016. *J. Lumin.* 169, 196–203.
- Schanda, J., Danyi, M., 1977. *Color Res. Appl.* 2, 161–163.
- Sharma, R.K., Ghose, R., 2015. *Ceram. Int.* 41, 967–975.
- Sharifalhoseini, Z., Entezari, M.H., Jalal, Razieh, 2015. *Ultrason. Sonochem.* 27, 466–473.
- Siddiquey, I.A., Furusawa, T., Sato, M., Bahadur, N.M., Alam, Md. M., Suzuki, N., 2012. *Ultrason. Sonochem.* 19, 750–755.
- Siraj, K., Hashmi, Jaweria Z., Shahzad, N., Muhammad, S.R., Saima, S., 2015. *Mater Today* 2, 5365–5372.
- Song, Y.L., Zhang, T.J., Du, H.J., Ji, P.F., Li, Y., Zhou, F.Q., 2016. *Mater. Lett.* 176, 139–142.
- Srikesh, G., Samson, A.N., 2016. *Ceram. Int.* 42, 5001–5010.
- Sun, Y., Guo, H., Zhang, W., Zhou, T., Qiu, Y., Xu, K., Zhang, B., Yang, H., 2016. *Ceram. Int.* 42, 9648–9652.
- Suresh, D., Nethravathi, P.C., Udayabhanu, Rajanaika, H., Nagabhushana, H., Sharma, S.C., 2015. *Mater. Sci. Semicond. Process* 31, 446–454.
- Toledo, P.V.M., Arend, L.N., Pilonetto, M., Costa Oliveira, J.C., Luhm, K.R., 2012. *J. Hosp. Infect.* 80, 351–353.
- Venkataravanappa, M., Nagabhushana, H., Darshan, G.P., Daruka Prasad, B., Vijayakumar, G.R., Premkumar, H.B., Udayabhanu, 2016. *Ultrason. Sonochem.* 33, 226–239.
- Vinod, K., Som, S., Kumar, Vijay, Vinay Kumar, O.M., Ntwaeaborwa, E., Coetsee, H.C. Swart, 2014. *Chem. Eng. J.* 255, 541–552.
- Wan, L., Li, J.F., Feng, J.Y., Sun, W., Mao, Z.Q., 2007. *Mater. Sci. Eng. B.* 139, 216–220.
- Wang, B., Zheng, Z.Q., Zhu, L.F., Yang, Y.H., Wu, H.Y., 2014. *Sens. Actuators, B: Chem.* 195, 549–561.
- Xiao, Y., Cao, M., 2016. *J. Power Sourc.* 305, 1–9.
- Yu, H., Fan, H., Wang, X., Wang, J., Cheng, P., 2015. *Optik.* 126, 4397–4400.
- Zhang, J., Xi, J., Ji, Z., 2012. *J. Mater. Chem.* 22, 17700–17708.